1.5-µm Optical Coherence Tomography for Quality Inspection of 3D-printed Scattering Phantoms

Janne Lauri
Optoelectronics and Measurement Techniques Research Unit
University of Oulu
Oulu, Finland
janne.lauri@oulu.fi

Tatiana Avsievich
Optoelectronics and Measurement Techniques Research Unit
University of Oulu
Oulu, Finland
tatiana.avsievich@oulu.fi

Oleksii Sieryi
Optoelectronics and Measurement Techniques Research Unit
University of Oulu
Oulu, Finland
olexii.siery@oulu.fi

Alexander Bykov
Optoelectronics and Measurement Techniques Research Unit
University of Oulu
Oulu, Finland
alexander.bykov@oulu.fi

Tapio Fabritius
Optoelectronics and Measurement Techniques Research Unit
University of Oulu
Oulu, Finland
tapio.fabritius@oulu.fi

***Abstract*—Additive manufacturing methods have an important role in the fabrication of novel tissue-mimicking phantoms to be used in the development and commercialization of imaging techniques. The quality of phantoms is crucial for their effective use in device evaluation and performance optimization. In this study, a new custom-built 1500 nm spectral domain optical coherence tomography (OCT) was applied for inspection of 3D printing quality of phantom materials and tumorous tissue phantoms. A commercial OCT operating at 930 nm was used for benchmarking. The results showed typical issues that occurred during 3D printing such as air bubbles, detached material contact, and non-homogeneous particle distribution. Results show that the OCT system, operating at longer wavelengths, achieves higher imaging depth in strongly scattering and water-free phantom materials, making it an improved tool for 3D-printed phantom validation.**

Keywords—SWIR OCT, 3D-printed tissue phantoms, non-destructive quality inspection

I. Introduction

Phantoms are widely used in biomedical research as a stable measurement object for development and calibration of new optical devices and validation of measurement techniques [1, 2, 3]. Stability is necessary to improve traceability of the measurement data which is very difficult with real biological samples. Material properties of phantoms are typically tuned for different imaging modalities, optical imaging techniques require specific absorption and scattering properties, whereas for ultrasound imaging, speed of sound and acoustic attenuation are more critical [4, 5, 6].

Additive manufacturing methods, in particular 3D printing, have enabled phantoms to become more complicated and realistic [7, 8]. Especially, the exploitation of multi-material 3D printing tools has expanded the possibilities of not only phantoms but functional structural elements in general [9]. By making use of phantom material development and high-accuracy 3D printing, complex multilayer structures with embedded channels mimicking the vessels within the tissue can be fabricated [10]. 3D design models can be very detailed representations of the target object; however, printing result is highly affected by chosen materials, printing parameters, and printer characteristics. Typical printing quality issues are e.g., non-homogeneous solid material filling (air gaps, non-uniform particle concentration), adhesion between different materials, discrepancy from the design geometry due to the material swelling or limitations in printing resolution. Thus, before using the printed sample as a tissue-like phantom, it must be validated by other measurement techniques before use.

Typically, optical methods are used to characterize phantoms that will be used for optical device development. Methods such as optical microscopy and transmission spectroscopy are suitable for surface characterization and determination of scattering and absorption parameters. However, often more detailed structural analysis is needed. Optical coherence tomography (OCT) is a well-established imaging modality in ophthalmology and biomedical field [11]. It can provide information about sample structure at the microscale, as well as parameters such as effective attenuation coefficient and group refractive index [12, 13, 14]. Since OCT detects mainly single scattered photons, it has a relatively limited imaging depth of <1 mm in highly scattering media [15]. Recent developments have introduced OCT systems that operate at longer wavelengths, which improve light penetration depth due to reduced light scattering [16, 17, 18]. The longer wavelengths typical have higher absorption in tissue due to the water, however, commonly used 3D printing materials have low water content. From such materials, durable and long-lasting tissue phantoms can be manufactured. The phantoms can mimic for instance histological samples that do not contain water when store in a biobank or embedded in paraffin.

In this study, we apply two OCT systems operating at 930 nm and 1500 nm wavelength to validate the 3D printing outcome of three different phantom materials. Two phantoms of histological blocks of tumorous tissue are fabricated according to a 3D model and further inspected by the OCT to validate the dimensions and printing quality.

II. Materials and Methods

A. Sample materials

Several types of UV-curable resins for 3D printing were used as materials for the phantoms. These resins are liquid polymers that solidify when exposed to ultraviolet light. For the phantom fabrication, we employ various resin types,

J.L. and T.A. were supported by European Regional Development Fund (PrintoDiSe, no. A76026). O.S. and A.B. acknowledge ATTRACT II META-HiLight project funded by the European Union's Horizon 2020 research and innovative programme under Grant Agreement No. 101004462

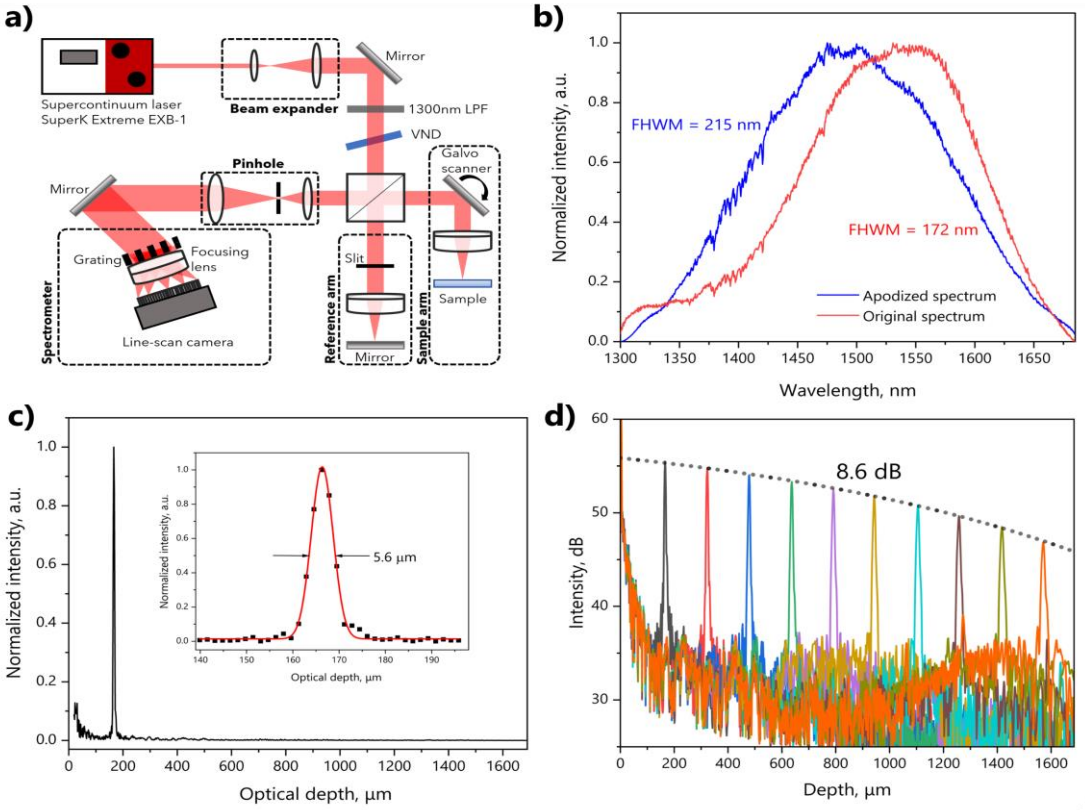

Fig. 1. Schematics of the developed SWIR-SDOCT system (a) and the detected original spectrum and the apodized spectrum (b). The PSF from the mirror reflection at the depth of 165 µm (c). The inset shows experimentally determined resolution. The sensitivity decay along the whole depth was 8.6 dB (d).

including standard ones commonly used in general-purpose 3D printing, and so-called engineering resins, which are characterized as clear or transparent flexible resins. The opaque resins with intrinsic scattering (Photocentric Flexible White and Zortax White Ivory) were utilized in their original form, directly as supplied. On the other hand, zinc oxide (ZnO) nanoparticles were added to the transparent resins (Formlabs Elastic and Formlabs Clear) to introduce scattering.

B. 3D printing

The process began with the creation of a three-dimensional digital model using computer-aided design (CAD) software. The phantom is then produced by direct 3D printing of the model, by stereolithography (SLA). This is one of the additive manufacturing techniques where a liquid resin is selectively cured layer by layer using ultraviolet (UV) light. The 3D printer follows the digital model's specifications and solidifies the resin to form the desired object.

The Anycubic Photon S desktop 3D printer that employs LCD-based SLA technology was used to fabricate the phantoms. Printing was performed at a specified layer thickness of 50 micrometers (µm). Once the printing was complete, the object was rinsed in a solvent bath to remove any excess resin, and then it was cured in a UV oven to fully solidify and strengthen the object.

As a result, three simple plain phantoms, each in the form of a monolithic square slab with a thickness of 1 mm, and two 2-component phantoms mimicking histological tissue blocks combining adipose and tumorous tissue of complex geometry were produced.

C. OCT systems

A commercial OCT (Hyperion, Thorlabs Inc.) and a laboratory-built high-resolution short-wavelength infrared (SWIR) spectral-domain OCT were used to characterize 3D printed phantoms. The Hyperion operates at a center wavelength of 930 nm and has an axial resolution of 5.8 µm in air.

The laboratory-built OCT, shown in Fig. 1a, operates at SWIR region 1300-1700 nm. A Supercontinuum laser (NKT Photonics SuperK Extreme EXB-1) light, attenuated by a neutral-density filter (ND3) and a longpass filter (FEL1300 - Ø1" Longpass Filter, with a cut-on wavelength of 1300 nm), was employed as the light source for the OCT system. The output power of the laser source was set to 9%. To minimize the focus spot size, the laser beam was expanded from 2 mm to 8 mm using a beam expander (BE04R/M). A variable neutral density (VND) filter was used for beam attenuation, controlling the power in both arms.

A 50/50 beamsplitter divided the incoming beam into the reference and sample arms. To mitigate chromatic dispersion and produce a focal spot size of approximately 11 µm, achromatic doublets (AC254-045-C) were incorporated into both arms. This configuration resulted in a depth of field (DOF) of 121 µm. A set of galvanometric mirrors (Thorlabs GVS012) enabled the scanning of the sample in the lateral plane. The lens position was adjusted relative to the mirrors such that the back focal plane was located roughly between the galvo mirrors. Using a USAF 1951 resolution target, the lateral resolution was confirmed to be $\Delta x = 11$ µm in the air.

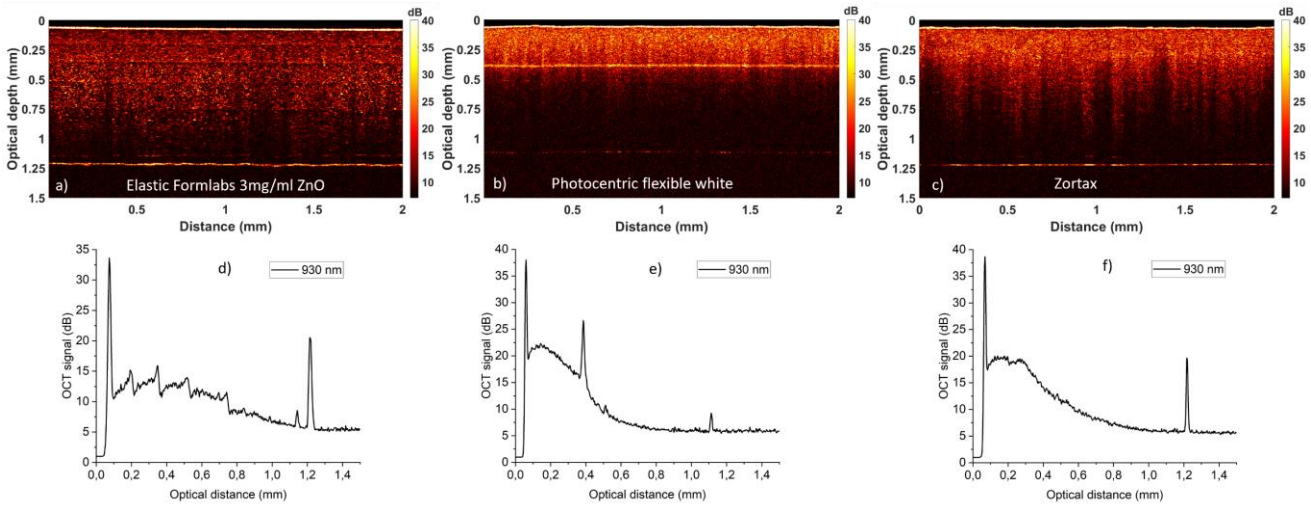

Fig. 2. B-scan images from the monolithic square slab samples: Elastic Formlabs (a), Photocentric flexible white (b) and Zortax white ivory (c). The averaged the A-scan signals are shown in (d-f).

To reject out-of-focus light from a sample, spatial filtering of the beam is performed by the achromatic doublet lens (AC254-050-C) focusing the 8 mm beam through a 25 µm pinhole. The beam is then collimated with a second lens (AC254-100-C) to 16 mm before continuing to a home-built spectrometer. The spectrometer is composed of a diffraction grating (600 l/mm @ 1550 nm, Wasatch Photonics Inc.), an achromatic doublet (AC254-100-C-ML), and a line scan camera (SU1024-LDH2, 12-bit, 92 kHz). The line rate of the camera was set to 43 kHz, which corresponds to the exposure time of 23 µs. The maximum scanning depth (in air) was 1.69 mm. A custom-written LabVIEW software was used to control data acquisition, the galvanometric mirrors, and the camera. The software performed interpolation of the spectrum followed by the Fourier transform to enable real-time monitoring of the measured sample. The data was saved as intensity images for post-processing with Matlab.

D. SWIR OCT performance

The spectral range covered by the camera detector spans $\Delta\lambda$ = 394 nm, extending from 1300 to 1694 nm. The spectrum's full-width at half-maximum (FWHM) is 172 nm, centered at a wavelength of λc = 1530 nm (Fig. 1b). Significant imaging enhancement is achieved through spectrum apodization, which results in a broadened FWHM of 215 nm and λc = 1496 nm (Fig. 1b).

Therefore, the theoretical axial resolution in the air was calculated to be 4.8 µm (for apodized spectrum, unapodized is 5.9 µm). The axial resolution of the SWIR-OCT system was experimentally measured from the point spread function (PSF) of the mirror reflection at depth z = 165 µm (Fig. 1c). The PSF was calculated from the apodized spectrum. The peak resolution in the air was 5.6 um. The sensitivity decay was 8.6 dB within the scanning range of 1.69 mm (Fig. 1d).

III. Results

A. Printed layers

To validate printing quality and estimate the applicability of the used printing parameters, cross-sectional scans (B-scans) along printed samples were acquired. The focus point of the sample arm lens, in both OCT systems, is adjusted to be at about 300 µm depth. Fig. 2a-c show B-scan images from the three printed structures (monolithic square slab) together with the averaged A-scans (Fig. 2d-f). For the Elastic Formlabs, with added ZnO particles, a clear layered structure is observed (Fig. 2a). The layers are also visible in the

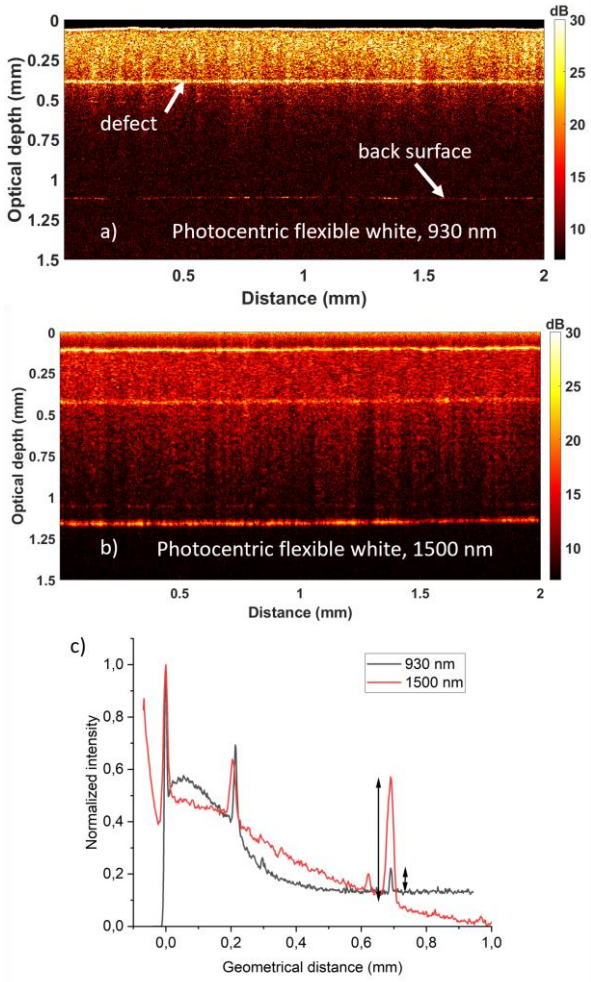

Fig. 3. B-scans from Photocentric flexible white at 930 nm (a) and 1500 nm (b). The comparison of the averaged A-scan signals (normalized) at 930 nm and 1500 nm (c). The double-sided arrows point the signal-to-background magnitude.

averaged A-scan (Fig. 2d) and slopes within the layers show a non-uniform distribution of particles. It is mainly due to the sedimentation of the added ZnO particles during the curing time of the resin. The Photocentric flexible white (Fig. 2b) has uniform scattering properties up to the depth of 300 µm (from the surface) indicating a homogeneous printing result. At a depth of 300 µm, there is a highly scattering interface. It is a defect that originates from an imperfect printing process and possible poor material attachment. After the interface, the signal from the 930 nm OCT is significantly reduced, and the peak from the backside of the printed layer is only just visible. For Zortax resin (Fig. 2c), scattering is uniform below the surface until the depth of 300 µm. At the deeper depths, local shadowing of the OCT signal is more prominent. This can be due to a nonhomogeneous material composition or microbubbles which increase scattering, and thus, cause strong attenuation of the signal.

Because of the poor imaging depth of 930 nm OCT, the Photocentric flexible white was imaged with the laboratory-built 1500 nm OCT. Because these phantom materials do not contain water, which has a higher attenuation coefficient of around 1500 nm, improved imaging depth is expected by utilizing longer wavelengths with reduced scattering. Fig. 3a and 3b show the B-scan images for 930 nm and 1500 nm respectively. For the 1500 nm OCT, the back surface is clearly distinguishable, and a noticeable increase in the backscattered signal below the defect is observed. The comparison between the averaged A-scan signals (normalized) of 930 nm and 1500 nm is shown in Fig. 3c. The optical distances are scaled with group refractive indexes to geometrical distances. The group refractive indexes were determined by dividing the optical thickness by the geometrical thickness measured by the precision caliber. For the 1500 nm OCT, a backscattered light is detected nearly up to the back surface. To quantify the difference between the two OCT setups, we determined signal-to-background values from the defect interface (at the depth of 200 µm) and the back surface. The values were determined from the non-normalized data. The 930 nm OCT had 2.6 times higher signal-to-background value at the defect (11.6 dB vs. 4.5 dB) which resulted the distinctive interface in Fig. 3a. At the back surface, the 1500 nm OCT demonstrated

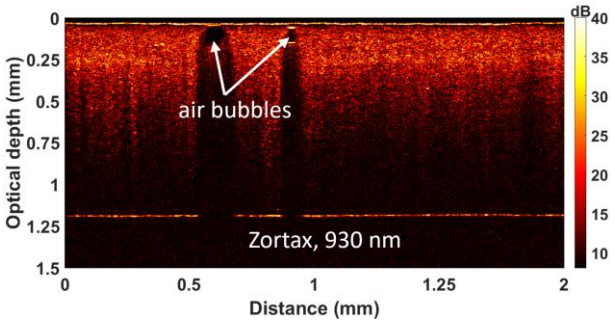

Fig. 4. B-scan from Zortax with 930 nm OCT. The air bubbles are located near the surface.

deeper imaging capabilities by 2.7 times higher signal-to-background value (3.4 dB vs. 9.4 dB). Another quantitative indication of higher imaging depth is a reduced attenuation coefficient, determined from the slope of the A-scan signal. Apparent attenuation coefficients were determined by linear fitting from the normalized signals (Fig. 3c) at the depth range from 100 µm to 180 µm. The values were 0.23 for 1500 nm OCT and 1.33 for 930 nm OCT which shows clear evidence for reduced scattering for 1500 nm OCT.

Often printing issues are related to unwanted air bubbles at random locations. This was also the case for Zortax sample, which had few air bubbles (Fig. 4). Air bubbles and highly scattering interfaces due to the faulty print should be detected before utilizing a phantom for new optical device development. Large air bubbles reflect light and hinder light penetration below the bubble. Similarly, for the strongly scattering interface, photons are detected at too shallow depts, correspondence to the modelling will be off, and therefore, signal interpretation becomes obscure. In addition, if the uniformity of the sample is not verified, further measurements of optical properties such as scattering and attenuation coefficients could show incorrect values, even though the original printing material composition is correctly tuned.

B. Phantoms of histological tissue blocks

Here we compared B-scan images to validate the printing result against the 3D model from the tumorous tissue. Fig. 5c

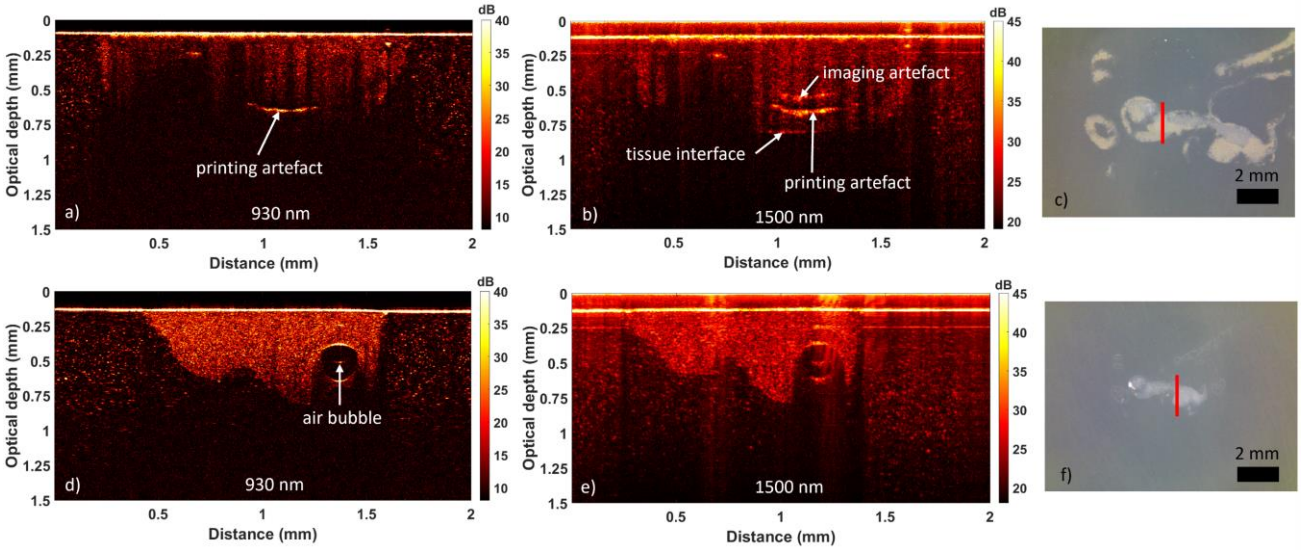

Fig. 5. B-scans from the 3D printed phantoms of histological tissue blocks with 930 nm (a, d) and 1500 nm (b, c) OCTs. The red lines show the B-scan locations in the larger (c) and smaller (f) tumorous tissue phantoms.

and 5f show images from the two printed structures that are differentiated only by the lateral scale. Due to the resolution of the printer and resin behaviour, scattering properties differ a lot from nearly homogenous (Fig. 5d) to highly anisotropic (Fig. 5a). These shadowed vertical lines (Fig. 5a-b) appear to start from the surface indicating that there is strong scattering at close to the surface masking the signal at deeper depths. Because of the masking effect, determination of the scattering properties at the shadowed lines is very limited. Both printed phantoms should have uniform thickness according to the model. However, the results show that the thickness is not constant (Fig. 5d). In a few locations, printing artifacts (Fig. 5a) and air bubbles (Fig. 5d) were observed. With the 1500 nm OCT, a deeper imaging depth was again achieved (Fig. 5b and 5e), and it was possible to see the tissue interface below the artifact. The deeper imaging depth is important for defining printed tissue thickness and validating it against the model.

IV. Conclusion

The high-resolution spectral domain OCT operating at the 1300-1700 nm wavelength region was introduced to characterize 3D printed phantoms. For benchmarking, we applied the 930 nm commercial OCT. The images showed typical printing quality issues, such as air bubbles and poor layer detachment. Since the printed materials had low water content, the benefits of using OCT at the longer wavelength region were evident. The improved imaging depth resulted in 2.7 times higher signal-to-background value of the back surface peak. In addition, the backscattered signal was obtained nearly throughout the sample. For the tumorous tissue phantoms, inconsistencies in properties, such as the layer thickness and the scattering uniformity, between the model and the printing outcome were observed. Those were strongly affected by the size of the print and could be due to the limited resolution of the printer. The scattering uniformity was difficult to confirm in the case where there was strong scattering point very close to the surface that caused high attenuation of backscattered signal at the deeper depths. With the 1500 nm OCT, it was possible to image the tumorous tissue interface that was not visible for 930 nm OCT.

The importance of quality inspection of novel tissue phantoms made from new 3D printer materials is evident and OCT is an excellent tool for that. The considered types of phantoms can be utilized for, e.g., polarization, spectral, and speckle contrast imaging, which provide 2D enface maps of specific measured parameters. Conventionally, these techniques do not offer specific depth selectivity, unlike OCT or other tomographic techniques. Thus, the presence of hidden, unexpected internal interfaces of uncontrolled shape and location or other possible printing artifacts within a measurement volume could lead to significant distortion in the measured parameters. This could compromise the calibration procedure or the verification of the theoretical models that are being considered. A printing outcome in relation to feature sizes of a model and material selection is one of the interesting future research areas, because just by scaling the model by the factor of 2, the results are completely different. Furthermore, the OCT signal also contains information about the attenuation coefficient and group refractive index that could be useful for determining optical properties and validating the phantom. Finally, the 1500 nm OCT imaging performance could be improved by taking advantage of fiber components and numerical compensation of a chromatic dispersion mismatch induced by the phantom.

References

[1] A. Cloonan, et al. “3D-Printed Tissue-Mimicking Phantoms for Medical Imaging and Computational Validation Applications,” 3D Print Addit. Manuf., vol. 1, no. 1, pp. 14-23, 2014.

[2] L. Christie, et al. “Review of imaging test phantoms,” J. Biomed. Opt., vol. 28, no. 8, p. 080903, 2023.

[3] G. Lamouche, et al. “Review of tissue simulating phantoms with controllable optical, mechanical and structural properties for use in optical coherence tomography,” Biomed. Opt. Express., vol. 3, no. 6, pp. 1381-98, 2012.

[4] W. Li, et al. “Polyvinyl chloride as a multimodal tissue-mimicking material with tuned mechanical and medical imaging properties,” Med. Phys., vol. 43, pp. 5577-5592, 2016.

[5] D. Ivanov, et al. “Suitability of low density materials for 3D printing of physical breast phantoms,” Phys. Med. Biol., vol. 63, no. 17, p. 175020, 2018.

[6] B. Pogue and M. Patterson, “Review of tissue simulating phantoms for optical spectroscopy, imaging and dosimetry,” J. Biomed. Opt., vol. 11, no. 4, p. 041102, 2006.

[7] M. Ommen, et al. “3D printed calibration micro-phantoms for super-resolution ultrasound imaging validation,” Ultrasonics, vol. 114, p. 106353, 2021.

[8] K. Wang, C. Ho, C. Zhang and B. Wang, “A Review on the 3D Printing of Functional Structures for Medical Phantoms and Regenerated Tissue and Organ Applications,” Engineering, vol. 3, no. 5, pp. 653-662, 2017.

[9] S. Myllymäki, E. Hannila, M. Kokkonen, H. Jantunen and T. Fabritius, “Design thinking-driven development of a modular X-Band antenna using multi-material 3D printing,” Int. J. Interact. Des. Manuf., pp. 1-10, 2023.

[10] C. N. Ionita, et al. “Challenges and limitations of patient-specific vascular phantom fabrication using 3D Polyjet printing,” in Proc SPIE Int Soc Opt Eng, 9038:90380M, San Diego, Mar 13, 2014.

[11] A. F. Fercher, W. Drexler, C. K. Hitzenberger and T. Lasser, “Optical coherence tomography – principles and applications,” Rep. Prog. Phys., vol. 66, p. 239–303, 2003.

[12] S. Chang and A. Bowden, “Review of methods and applications of attenuation coefficient measurements with optical coherence tomography,” J. Biomed. Opt., vol. 24, no. 9, pp. 1-17, 2019.

[13] L. Neubrand, T. van Leeuwen and D. Faber, “Accuracy and precision of depth-resolved estimation of attenuation coefficients in optical coherence tomography,” J. Biomed. Opt., vol. 28, no. 6, p. 066001, 2023.

[14] J. Lauri, C. Liedert, A. Kokkonen and T. Fabritius, “Effect of solvent lamination on roll-to-roll hot-embossed PMMA microchannels,” Mater. Res. Express, vol. 6, no. 7, p. 075333, 2019.

[15] J. Lauri, et al. “Online measurement of floc size, viscosity, and consistency of cellulose microfibril suspensions with optical coherence tomography,” Cellulose, vol. 28, p. 3373–3387, 2021.

[16] I. Zorin, et al. “Mid-infrared optical coherence tomography as a method for inspection and quality assurance in ceramics additive manufacturing,” Open Ceramics, vol. 12, p. 100311, 2022.

[17] U. Sharma, E. Chang and S. Yun, “Long-wavelength optical coherence tomography at 1.7 μm for enhanced imaging depth,” Opt. Express, vol. 16, no. 23, pp. 19712-23, 2008.

[18] M. Yamanaka, N. Hayakawa and N. Nishizawa, “High-spatial-resolution deep tissue imaging with spectral-domain optical coherence microscopy in the 1700-nm spectral band,” J. Biomed. Opt., vol. 24, no. 7, pp. 1-4, 2019.